Incoherent Active Convolved Illumination Enhances the Signal-to-Noise Ratio for Shot Noise: Experimental Evidence

Wyatt Adams, Anindya Ghoshroy, and Durdu Ö. Güney

Phys. Rev. Applied **18**, 064080 — Published 26 December 2022

DOI: 10.1103/PhysRevApplied.18.064080

Incoherent active convolved illumination enhances the signal-to-noise ratio for shot noise: experimental evidence

Wyatt Adams[1,2], Anindya Ghoshroy[1,3], and Durdu Ö. Güney[1*]
[1] *Department of Electrical and Computer Engineering , Michigan Technological University, 1400 Townsend Dr, Houghton, MI 49931-1295, USA*
[2] *Ansys, Inc., 2600 Ansys Dr, Canonsburg, PA 15317, USA and*
[3] *Caltech Optical Imaging Laboratory, Andrew and Peggy Cherng Department of Medical Engineering and Department of Electrical Engineering, California Institute of Technology, 1200 E. California Blvd., Pasadena, CA 91125, USA*
(Dated: November 25, 2022)

Imaging is indispensable for nearly every field of science, engineering, technology, and medicine. However, measurement noise and stochastic distortions pose fundamental limits to accessible spatiotemporal information despite impressive tools such as SIM, STORM/PALM, and STED microscopy. How to combat this challenge ideally has been an open question for decades. Inspired by a '*virtual gain*' technique to compensate losses in metamaterials, '*active convolved illumination*' has been recently proposed to significantly improve the signal-to-noise ratio, hence data acquisition. In this technique, the light pattern of the object is superimposed with a correlated auxiliary pattern, the function of which is to reverse the adverse effect of losses, noise, and random distortion based on their spectral characteristics. Despite enormous implications in statistics, any experimental evidence verifying the theory of this novel technique has been lacking to date. We find experimentally that the active convolved illumination does not only boost the resolution limit and image contrast, but also the resistance to pixel saturation. The results confirm the previous theories and open up new horizons in a wide range of disciplines from atmospheric sciences, seismology, biology, statistical learning, finance, and information processing to quantum noise beyond the fundamental boundaries.

I. INTRODUCTION

Imaging is an indispensable tool in the toolbox of nearly every field of science, engineering, technology, and medicine. Unfortunately, encoding the desired information into electromagnetic waves imposes a limit to the performance of imaging systems at the outset – the detection of the fields by the interaction of photons (the light signal) and matter (the light detector) means that the signal-to-noise ratio (SNR) for long exposures will always be limited physically by shot noise. A naïve analysis would reveal that adding up more photons in the detector would lead to higher SNR. This is true, however typically (e.g., for incoherent light), the magnitude of the transfer function for an imaging system with an unobstructed pupil decreases with increasing spatial frequency [1]. It follows that the spectral SNR then also decreases with increasing spatial frequency, since the shot noise variance is constant in the spatial frequency domain [2–4]. Consequently, adding up more photons blindly does not lead to much increase for the SNR of high spatial frequencies. One also does not have the freedom to arbitrarily increase the number of photons collected, since at some point the detector will become saturated. Each specific imaging modality will have its specific limitations. For example, in fluorescence imaging only a certain exposure can be obtained before photobleaching occurs and high intensity becomes detrimental for live specimen.

Subwavelength optical engineering through metamaterials and metasurfaces offers unprecedented opportunities in a wide range of applications such as superresolution imaging [5–9], photolithography [10, 11], wireless and optical communications [12, 13], multifunctional and flat optics and photonics [14–16], metalenses [17], intelligent metaphotonics [18], light detection and ranging [19], autonomous vehicles [20], and quantum information [21, 22]. However, the photon losses hinder their further viability [23–25]. Inspiration from research in loss compensation for metamaterials and plasmonics employing '*virtual gain*' [25–28] led us to propose a unique perspective on the noisy imaging problem [2, 27, 29–34]. The fundamental resolution limit to superresolving lenses is not determined by the diffraction limit, but rather by a shot noise limit, i.e. where the shot noise overcomes the transfer function in the spatial frequency domain [4, 35–37]. How to tackle this problem ideally has been an open question for decades [36–40]. The *active convolved illumination* (ACI) technique has recently been proposed theoretically as a ubiquitous noise and distortion mitigation scheme to improve the image SNR by systematically manipulating the image spectrum depending on the underlying stochastic behavior [2, 27, 31–34]. Popular techniques to improve image resolution or SNR are structured illumination microscopy (SIM) [3, 41–44], stimulated emission depletion (STED) microscopy [41, 45, 46], stochastic optical reconstruction microscopy/photoactivated localization microscopy (STORM/PALM) [41, 47, 48], and computational methods [36–40, 49, 50] including machine learning [35, 51]. An interesting method for far-field imaging with a constant '*photon budget*' (i.e., a con-

* Corresponding author: dguney@mtu.edu

stant number of photons in the object plane), based on a split-pupil-optimization, has recently been put forward to break the SNR limit imposed by Fermat's principle [4]. However, ACI operates down at the physical layer and enhances data acquisition, thus it is expected to benefit both conventional and novel approaches.

The working principle of the ACI technique is illustrated in Fig. 1. As shown in Fig. 1(a), most imaging systems suffer from various mechanisms of signal photon loss such as impedance mismatch, absorption, scattering, diffraction, and noise. This, in general, results in a low-fidelity information transfer from the object plane to the receiver plane. It was hypothesized that the ACI could overcome the loss of information as depicted in Fig. 1(b) [2, 27, 31, 32]. The light pattern which forms the object (black line) is superimposed with an auxiliary pattern (blue line) correlated with the object. Therefore, the light pattern on the same object plane differs from the object. The purpose of the auxiliary is to manipulate the image spectrum to compensate the adversary photons, so that the object pattern is transferred through the system unscathed. The auxiliary pattern is typically found by characterizing the spectral distribution of noise obtained from the reference imaging system in Fig. 1(a) [2], as the noise poses the fundamental limit to accessible spatial information [4, 35, 36]. The auxiliary and object patterns can also be implemented as an inherently single entity (i.e., from a single undivided source) in the object plane as shown in Fig. 1(c) [33]. The negative values for the auxiliary is not precluded. For incoherent imaging this physically means the energy is reduced at those locations, which is indeed useful to prevent excessive noise, long average exposure, and pixel saturation. Another equivalent implementation, which is discussed theoretically and realized experimentally in the present work, is illustrated in Fig. 1(d). In contrast with Figs. 1(b) and 1(c), where the image spectrum is manipulated from the object plane only, here instead, it is manipulated from both the object plane, via a varied exposure time or intensity, and pupil plane simultaneously. Utilizing the pupil plane aids in a simple construction of an embedded auxiliary (i.e., embedded with the original object pattern as a single entity) in the object plane. In this case, the embedded auxiliary is simply proportional to the original object pattern.

The previous works on the foundations of ACI [2, 27, 31–34], along with further inspiration from other research on noisy far-field imaging [3, 4], led us to construct the current work, which presents the first experimental evidence for the theory of ACI. Following the implementation sketched in Fig. 1(d), we find for incoherent light that by suppressing the detection of the high-SNR spatial frequency harmonics in an object, while amplifying the magnitude of those with low SNR, the resulting image can have large SNR for previously low-SNR spatial frequencies, due to a prudent control of the flat overall noise level dictated by the Poisson distribution. This does not only manage the exposure time efficiently, but also leads to enhanced image resolution and contrast beyond what is possible with common post-processing.

The previous body of literature [2, 27, 31–34] on ACI has been only theoretical and typically utilized a high spatial frequency passband function, in conjunction with an increased exposure, to enhance the resolution performance of thin metal films acting as near-field plasmonic superlenses [2, 31–34]. This passband function was used to not only compensate the losses inherent in the metal film (i.e., virtual gain), but also to improve the image spectrum SNR similar to what we have shown in this work at far-field. This imaging method has been called [32] '*active convolved illumination*' for a couple reasons. First, the term 'active' was chosen since an added energy [33] (though not strictly necessary) was used to obtain enhancement over the control (a bare superlens). Secondly, the term 'convolved' was chosen since the applied passband function is physically convolved with the fields emanating from the object. For coherent illumination, this passband function can be realized by a hyperbolic metamaterial (HMM) [33, 34]. While there is no Fourier plane in the near-field configuration, the HMM can modify the Fourier components of the incident evanescent waves by its dispersion. In this case, the pupil function can then simply be thought of as the coherent transfer function of the cascaded HMM-superlens system and the SNR for the large spatial frequencies is enhanced with respect to the control.

Below, first a theory of ACI for incoherent light is presented that shows how to improve the SNR for the high spatial frequencies (i.e., low-SNR components) of an image obtained from an object illuminated with incoherent light. The theory is implemented in numerical simulations to predict the resolution enhancement, and experimental images are collected using a low numerical aperture imaging system to confirm the predictions. The end result is an image with higher resolution and improved contrast as compared to the control image. It is also shown that ACI can help prevent pixel saturation for longer exposures. The experimental work here confirms that the theories of ACI are, in fact, both consistent with real noisy optical signals, and can be extended to conventional far-field imaging systems and potentially to complex systems with different noise and distortion characteristics. A detailed understanding of random processes in the Fourier domain, crucial for the implementation of the ACI, and the subsequent development of the auxiliary pattern (Fig. 1(b)) or the equivalent combined light pattern for the object (Figs. 1(c) and 1(d)), immune to such distorting effects, may in general open multiple avenues of research. It may lead to a generalized theory of randomly distorted systems pervading a wide range of disciplines from atmospheric sciences, seismology, finance, and biology to the mesoscopic physics of noisy quantum systems.

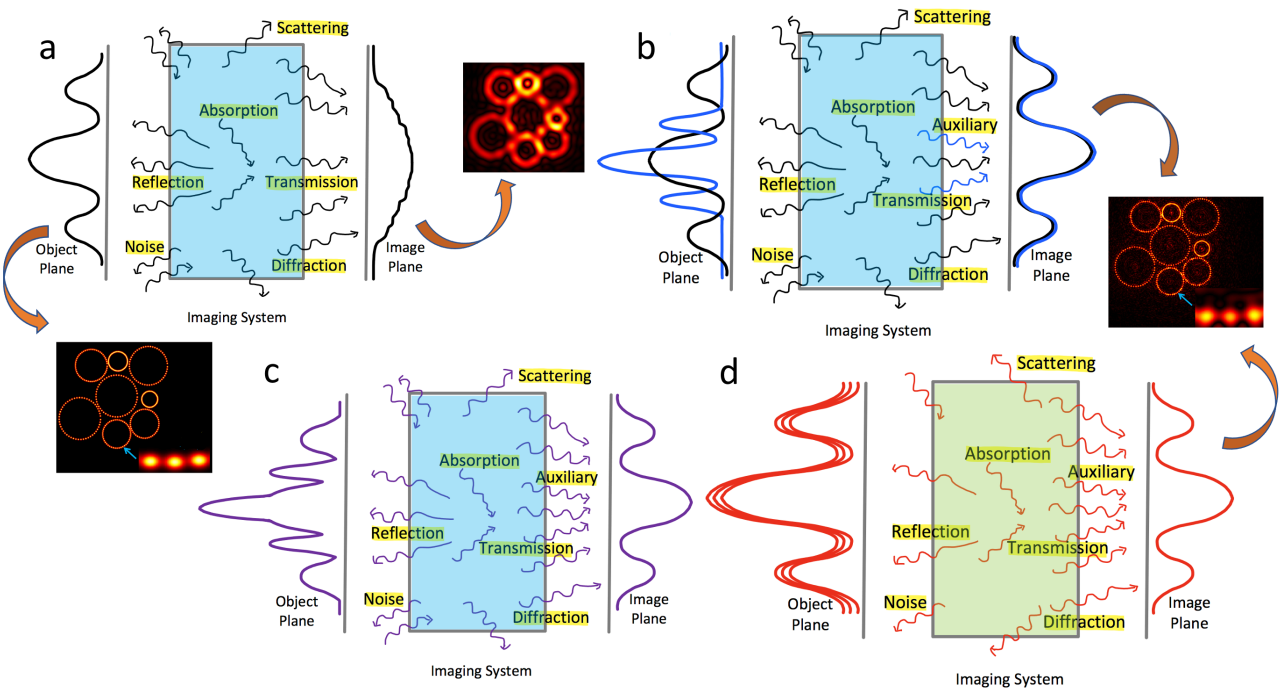

FIG. 1. Working principle of the active convolved illumination technique. (a) Most imaging systems suffer from loss of information due to physical processes such as reflection, absorption, scattering, diffraction, and noise. This results in an image with a poor resolution and contrast. (b) In the ACI technique, the light pattern forming the object (black line) is superimposed with an auxiliary pattern (blue line), the purpose of which is to compensate the adversary photons that cause the information leakage from the system. The auxiliary is correlated with the object and based on typically the underlying spectral noise distribution. The result is a remarkable acquisition of data, hence high-fidelity image. (c, d) Equivalent to part (b) except that the auxiliary and object patterns are implemented as an inherently single entity by utilizing (c) the object plane only or (d) both the object and pupil planes simultaneously instead. The implementation in part (d) may lead to a greatly simplified embedded auxiliary in the object plane, hence a simple physical construction.

II. THEORETICAL MODEL

Let us consider a uniform beam of spatially incoherent, narrowband light with photon flux density (photons/$m^2 \cdot s$) striking a planar, transmissive object. After passing through the object, the light has spatial variations and the resulting transmitted photon flux density is given by $O(\mathbf{r})$, with $\mathbf{r} \in \mathbb{R}^2$ denoting the position coordinate on the plane. The process of mapping this light distribution with an imaging system can be represented by a convolution

$$I(\mathbf{r}) = H(\mathbf{r}) * O(\mathbf{r}), \tag{1}$$

where $I(\mathbf{r})$ is the photon flux density on the image plane, $H(\mathbf{r})$ is the unshifted point spread function (PSF) of the imaging system, and $*$ denotes the convolution. Here it should be noted that $I(\mathbf{r})$, $O(\mathbf{r}) \in \mathbb{R}_{\geq 0}$ since they represent flux densities and not complex fields. Applying the convolution theorem and using the normalized image and object spectra, $\tilde{I}(\mathbf{k})$ and $\tilde{O}(\mathbf{k})$, respectively, Eq. (1) gives

$$\tilde{I}(\mathbf{k}) = \tilde{H}(\mathbf{k})\tilde{O}(\mathbf{k}), \tag{2}$$

where $\tilde{H}(\mathbf{k})$ is the optical transfer function (OTF) of the imaging system [1]. In general $\tilde{I}(\mathbf{k})$, $\tilde{H}(\mathbf{k})$, $\tilde{O}(\mathbf{k}) \in \mathbb{C}$. For later use, we define $|\tilde{H}(\mathbf{k})|$ as the modulation transfer function (MTF).

Eqs. (1) and (2) assume continuous signals in position and reciprocal space. To incorporate practical detection of the deterministic signal $I(\mathbf{r})$, let us consider the case where we collect an image on the image plane using a photoelectric detector with n_p pixels. The center of the p^{th} pixel ($p \in \mathbb{Z}_+$) is at $\mathbf{r}_p = (x_i, y_j)$, and the pixels are rectangular with side lengths Δx and Δy along the x and y dimensions, respectively. Then, at the p^{th} pixel, the expected number of detected photons is given by

$$\begin{aligned} \bar{I}_p &= \eta T \int_{A_p} I(\mathbf{r}) d^2\mathbf{r} \\ &= \eta T \int_{y_j-\Delta y/2}^{y_j+\Delta y/2} \int_{x_i-\Delta x/2}^{x_i+\Delta x/2} I(x,y) dx dy \\ &\approx \eta T \Delta x \Delta y I(x_i, y_j), \end{aligned} \tag{3}$$

where η is the quantum efficiency of the pixel and T is the exposure time or integration time. The approximation in the third line of Eq. (3) assumes that the signal $I(\mathbf{r})$ is slowly varying across the area of the pixel, i.e. the signal

is well sampled. Since Eq. (3) describes a sampling of a spatial distribution of discrete particles (photons), there will be an intrinsic randomness due to shot noise in the photon signal $I_{p,\gamma}$. In this case, the probability mass function (PMF) is

$$\mathcal{P}\left(I_{p,\gamma}|\bar{I}_p\right) = \frac{\left(\bar{I}_p\right)^{I_{p,\gamma}}}{I_{p,\gamma}!}e^{-\bar{I}_p}. \tag{4}$$

This is of course coming from the fact that the counting of discrete particles at a constant rate follows a Poisson distribution, for which

$$\mathrm{Var}(I_{p,\gamma}) = \bar{I}_p. \tag{5}$$

In most photoelectronic imaging detectors, such as complementary metal-oxide-semiconductor (CMOS) or charge-coupled device cameras, there are primarily two sources of noise. The first is due to the statistics of Eq. (4), the shot noise which is dependent on the photon signal. The second is noise from the readout electronics, which is independent of the photon signal. We can then write the detected signal as

$$I_p = \bar{I}_p + N_{p,\gamma} + N_{p,e}, \tag{6}$$

where $N_{p,\gamma}$ is a discrete random variable representing the shot noise with PMF described by Eq. (4), and $N_{p,e}$ is a discrete random variable representing the electronic readout noise.

In order to show how the noise addition in Eq. (6) affects the image spectrum, we compute the discrete Fourier transform

$$\begin{aligned}
\tilde{I}_q &= \sum_p I_p e^{-i2\pi\mathbf{k}_q\cdot\mathbf{r}_p} \\
&= \sum_p (\bar{I}_p + N_{p,\gamma} + N_{p,e}) e^{-i2\pi\mathbf{k}_q\cdot\mathbf{r}_p} \\
&= \sum_p \bar{I}_p e^{-i2\pi\mathbf{k}_q\cdot\mathbf{r}_p} + \sum_p N_{p,\gamma} e^{-i2\pi\mathbf{k}_q\cdot\mathbf{r}_p} \\
&+ \sum_p N_{p,e} e^{-i2\pi\mathbf{k}_q\cdot\mathbf{r}_p} \\
&= \tilde{\bar{I}}_q + \tilde{N}_{q,\gamma} + \tilde{N}_{q,e},
\end{aligned} \tag{7}$$

where $q \in \mathbb{Z}_+$ and $\{\mathbf{k}_q = (k_{x,l}, k_{y,m}) \mid 1 \le q \le n_p\} \subset \{\mathbf{k} \in \mathbb{R}^2\}$ is the Fourier space corresponding to the pixelated position space $\{\mathbf{r}_p \mid 1 \le p \le n_p\}$. We then consider the statistical properties of $\tilde{N}_{q,\gamma}$ and $\tilde{N}_{q,e}$. Since the shot noise variance is known from Eq. (5) (replacing $I_{p,\gamma}$ with $N_{p,\gamma}$) and we can assume the pixels are statistically independent, we can write [2–4]

$$\begin{aligned}
\mathrm{Var}(\tilde{N}_{q,\gamma}) &= \mathrm{Var}\left(\sum_p N_{p,\gamma} e^{-i2\pi\mathbf{k}_q\cdot\mathbf{r}_p}\right) \\
&= \sum_p \mathrm{Var}(N_{p,\gamma}) |e^{-i2\pi\mathbf{k}_q\cdot\mathbf{r}_p}|^2 \\
&= \sum_p \bar{I}_p = n_\gamma,
\end{aligned} \tag{8}$$

where n_γ is the total expected number of photons in the entire image. In words, Eq. (8) states that the variance in Fourier space is constant, and is controlled by the total expected number of photons collected on the detector. We can write a similar equation for the readout noise [3],

$$\begin{aligned}
\mathrm{Var}(\tilde{N}_{q,e}) &= \mathrm{Var}\left(\sum_p N_{p,e} e^{-i2\pi\mathbf{k}_q\cdot\mathbf{r}_p}\right) \\
&= \sum_p \mathrm{Var}(N_{p,e}) |e^{-i2\pi\mathbf{k}_q\cdot\mathbf{r}_p}|^2 = \sum_p \sigma_{p,e}^2,
\end{aligned} \tag{9}$$

where $\sigma_{p,e}^2$ is the readout noise variance at pixel p and again the assumption is made that the pixels are statistically independent. Let us also assume that $\sigma_{p,e}^2 = \sigma_e^2$, meaning every pixel has similar electrical performance in terms of noise. Then Eq. (9) becomes

$$\mathrm{Var}(\tilde{N}_{q,e}) = n_p \sigma_e^2. \tag{10}$$

Therefore, the spectral readout noise variance is also a constant, and scales linearly with the number of pixels. For modern cameras, the readout noise is usually minimal such that it is neglected, though we keep it here for completeness.

From imaging theory, we know that the OTF of an incoherent imaging system is given by the normalized autocorrelation [1] of the system's pupil function $\tilde{P}(\mathbf{k})$, or

$$\tilde{H}(\mathbf{k}) = \frac{\int \tilde{P}(\boldsymbol{\kappa})\tilde{P}^*(\boldsymbol{\kappa}-\mathbf{k})d^2\boldsymbol{\kappa}}{\int |\tilde{P}(\boldsymbol{\kappa})|^2 d^2\boldsymbol{\kappa}}. \tag{11}$$

In the discrete notation described above, we can write

$$\tilde{H}_q = \frac{\sum_{\boldsymbol{\kappa}} \tilde{P}_{\boldsymbol{\kappa}} \tilde{P}^*_{\boldsymbol{\kappa}-\mathbf{k}_q}}{\sum_{\boldsymbol{\kappa}} |\tilde{P}_{\boldsymbol{\kappa},o}|^2} = \alpha \tilde{P}_q \star \tilde{P}_q, \tag{12}$$

where $\tilde{P}_{\boldsymbol{\kappa},o}$ is a reference pupil, α is the normalization constant, and $\tilde{P}_q$ is the pupil function in the discrete notation. To normalize Eq. (12), the reference pupil is conventionally chosen as the pupil itself, making the DC pixel of $\tilde{H}_0 = 1$, similar to Eq. (11). However we define a reference pupil in Eq. (12) in order to later directly compare two different pupil functions. Consider an incoherent imaging system in air with maximum resolvable spatial frequency $k_{max} = 2\mathrm{NA}k_0$, where NA is the numerical aperture, $k_0 = 1/\lambda_0$, and λ_0 is the center free space wavelength of the illumination source. The pupil function is assumed to have circular symmetry about the optical axis (which is along z-direction) and we define it as

$$\tilde{P}_q = \begin{cases} 1 & \text{if } k_- \le |\mathbf{k}_q| \le k_+ \\ 0 & \text{otherwise,} \end{cases} \tag{13}$$

where $k_- \ge 0$ and $k_- < k_+ \le k_{max}/2$. From Eq. (13) we can see that setting $k_- = 0$ and $k_+ = k_{max}/2$ gives a typical diffraction-limited imaging system with open pupil.

We choose this case as our reference pupil $\tilde{P}_{q,o}$. However, if we make k_- nonzero, we introduce an obstruction in the central portion of the pupil, which has the effect of lowering the overall transmission with respect to the reference pupil, and also preferentially reinforcing larger spatial frequencies with respect to the smaller ones in comparison to the reference pupil.

An important metric for an imaging system is its ability to discern image spectrum content from noise, or its spectral SNR. To relate the pupil function to the spectral SNR, we first use Eqs. (2) and (12), without normalization, to rewrite the expected image spectrum as

$$\tilde{\bar{I}}_q = \left[\beta \tilde{P}_q \star \tilde{P}_q\right] \tilde{O}_q = \tilde{\mathcal{H}}_q \tilde{O}_q, \tag{14}$$

where $\beta \tilde{P}_q \star \tilde{P}_q = \tilde{\mathcal{H}}_q$ is the unnormalized OTF and β is a new constant. Using a standard definition of SNR, we then can write

$$\begin{aligned} \mathrm{SNR}_q &= \frac{|\tilde{\bar{I}}_q|}{\sqrt{n_\gamma + n_p \sigma_e^2}} = \frac{\left|\left[\beta \tilde{P}_q \star \tilde{P}_q\right] \tilde{O}_q\right|}{\sqrt{n_\gamma + n_p \sigma_e^2}} \\ &= \frac{\left|\tilde{\mathcal{H}}_q \tilde{O}_q\right|}{\sqrt{n_\gamma + n_p \sigma_e^2}} \end{aligned} \tag{15}$$

as the image spectrum SNR. In Eq. (15), the numerator is the expected image spectrum, which can be engineered by manipulation of the pupil function, and the denominator is the total standard deviation of the signal from the photonic and electronic noise terms in Eqs. (8) and (9). An obvious consequence of Eq. (15) is that reducing n_γ will decrease the constant noise floor in the image spectrum. The signal in the numerator will also decrease similarly, but can be engineered through $\tilde{P}_q$ to enhance different portions of the spectrum. Conversely, increasing n_γ will increase the constant noise floor, but this will also increase the signal. If the readout noise is neglected in Eq. (15), SNR_q will then theoretically increase with $\sqrt{T}$ (Eq. (3)). Interestingly, if one can additionally manipulate the pupil function to amplify certain spectral regions, further improvement in SNR_q becomes possible in those regions beyond original shot noise limited signal. Engineering the system to preferentially pass a certain band or bands of the image spectrum, while keeping the overall noise unchanged can also improve SNR_q for the selected regions. To put the latter scenario into analogy, we are given a '*photo-budget*' (i.e., a constant number of photons in the image plane) [52] n_γ, and we can freely decide how to spend that budget in the image spectrum via $\tilde{P}_q$ so that we achieve an improved SNR for certain spatial frequencies. Boosting SNR with such spectrum manipulation scenarios above considering the underlying noise statistics forms the essence of ACI and is the central theme of this work. The relation of these processes with the auxiliary pattern in Figs. 1(b) and 1(c) can be explained as follows.

Let $\tilde{\mathcal{H}}_{q,o}$ and $\tilde{\mathcal{H}}_{q,A}$ be the unnormalized OTFs for the imaging systems without (i.e., reference) and with ACI, respectively. Then, the expected image spectrum obtained by the auxiliary component becomes

$$\begin{aligned} \tilde{\bar{I}}_{q,aux} &= \tilde{\mathcal{H}}_{q,A}\tilde{O}_q - \tilde{\mathcal{H}}_{q,o}\tilde{O}_q = \tilde{h}_q \tilde{\mathcal{H}}_{q,o}\tilde{O}_q - \tilde{\mathcal{H}}_{q,o}\tilde{O}_q \\ &= \tilde{\mathcal{H}}_{q,o}(\tilde{h}_q - 1)\tilde{O}_q, \end{aligned} \tag{16}$$

where we define the virtual gain $\tilde{h}_q = \tilde{\mathcal{H}}_{q,A}/\tilde{\mathcal{H}}_{q,o}$ with $\tilde{\mathcal{H}}_{q,o} \neq 0$. Therefore, the auxiliary pattern spectrum corresponding to Fig. 1(b) and the combined object spectrum and embedded auxiliary corresponding to Fig. 1(c) can be, respectively, expressed as

$$\tilde{O}_{q,aux} = (\tilde{h}_q - 1)\tilde{O}_q, \tag{17}$$

$$\tilde{O}_{q,A} = \tilde{h}_q \tilde{O}_q, \tag{18}$$

which are both correlated with the object. $\tilde{\mathcal{H}}_{q,A}$ in Eq. (16) is also known as the '*active transfer function*' (ATF) [2] and proportional to the exposure time. If the ATF leads to amplification at some spatial frequencies with respect to the reference system, this implies virtual gain in that spectral region.

Similarly, to express the embedded auxiliary spectrum $\tilde{O}_{q,aux}$ of Fig. 1(d), we start with the transformation equation for the expected image spectrum

$$\tilde{\bar{I}}_q = \tilde{H}_{q,a}(\tilde{O}_q + \tilde{O}_{q,aux}) = \tilde{H}_{q,A}\tilde{O}_q, \tag{19}$$

where $\tilde{H}_{q,a}$ is the unnormalized OTF of the imaging system in Fig. 1(d) when the exposure time is kept the same as the reference (Fig. 1(a)). Then, we find

$$\tilde{O}_{q,aux} = (\tau - 1)\tilde{O}_q \tag{20}$$

where $\tau = \tilde{H}_{q,A}/\tilde{H}_{q,a}$ is the virtual gain for this system, which simply turns out to be the factor of increase in exposure time. Since both systems (Figs. 1(c) and 1(d)) are designed to produce the same expected image spectrum $\tilde{H}_{q,A}\tilde{O}_q$, the spectral noise variance is also the same (Eq. (8)). Therefore, both implementations equivalently manipulate the image spectrum using different auxiliaries. It is needless to say that intensity has a similar role as exposure time and we primarily consider the latter in our analysis. As described in the upcoming section, the ACI in this work (Fig. 1(d)) is experimentally realized with the modified pupil (i.e., via $\tilde{H}_{q,a}$ in Eq. (19)) and the simple embedded auxiliary in Eq. (20).

III. EXPERIMENT

In order to implement the above spectral SNR manipulation into an experimental imaging system, we simply need access to the Fourier space in order to manipulate the pupil function. Therefore, we chose to construct a typical $4f$ system with no magnification as shown in Fig. 2(a) in order to simplify the analysis and experiment.

The experimental setup in Fig. 2(a) images an object (target) illuminated by a narrowband incoherent

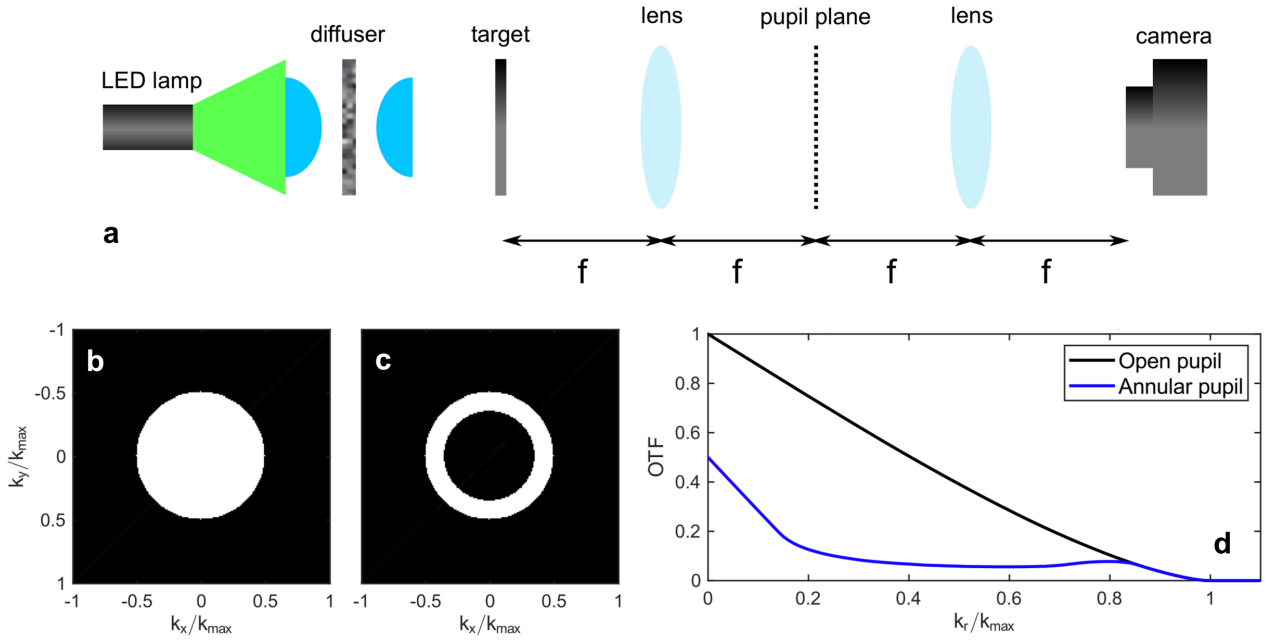

FIG. 2. Imaging experiment configuration, pupils used in the experiment, and the corresponding OTFs. (a) A diffused light emitting diode (LED) source illuminates an imaging target, which is then processed by a $4f$ system consisting of two achromatic doublet lenses and a transparency in the pupil plane with a focal length of $f = 38.1$ cm. The images are detected with a CMOS camera. (b) Open (reference) and (c) annular pupils with (d) corresponding OTFs calculated from Eq. (12) as a function of radial spatial frequency $k_r = \sqrt{k_x^2 + k_y^2}$. Both pupils have $k_+ = k_{max}/2$. In part (b), $k_- = 0$ and in part (c), $k_- = k_{max}/2\sqrt{2}$. In the actual experiment, we chose an outer pupil diameter of 5 mm for parts (b) and (c), making NA= 0.0066. In part (d) the OTF for the annular pupil was normalized with respect to open pupil to illustrate their relative transfer characteristics.

light source (Thorlabs LIU525B) at 525 nm wavelength. Before hitting the target, the light is focused onto a diffuser in order to decrease the spatial coherence and to avoid imaging the light source onto the pupil plane. Then the light is roughly collimated by a second lens before hitting the target. The light distribution exiting the target is transferred through an achromatic-doublet lens (Space Optics Research Labs) with a focal length of $f = 38.1$ cm. On the pupil plane, a pupil transparency is placed that has either a circular or annular opening, as shown in Figs. 2(b) and 2(c). For all the images, we chose an outer pupil diameter of $d = 5$ mm, making NA= 0.0066 using the formula NA= $d/2f$. The transparencies were printed with a photoplotter onto transparent plastic sheets, then cut out and mounted in standard optical mounts. After passing through the pupil plane, the light is again transferred through a second identical achromatic-doublet which then focuses the resulting image onto a CMOS camera (Thorlabs DCC1645C).

The goal of this experiment was to show directly an enhancement in image resolution by modifying the pupil and exposure time to improve SNR_q for the largest spatial frequencies in accordance with Eq. (15). This led to an annular pupil configuration. The ACI here is then simply implemented with annular pupil and variable photon exposure, and the reference system with open pupil, using incoherent light at 525 nm wavelength (Figs. 2(b) and 2(c)). The relative transfer characteristics of the open and annular pupils are plotted in Fig. 2(d). However, it should be emphasized that the concepts presented should be generally applicable to any imaging system which is linear and shift-invariant, provided there is a mechanism with which to manipulate the Fourier content of the light.

To show quantitatively the improvement in the resolution performance afforded by the annular pupil configuration with modified exposure over the open pupil, we replaced the resolution target with a 10 μm diameter pinhole. Since this diameter is below the diffraction limit for the chosen numerical aperture defined by k_+ and f, the resulting image of the pinhole gives the unshifted PSF of the imaging system at an arbitrary scale. These PSF images were taken with both the open and annular pupil transparencies with varying exposure times. From these images, the OTFs and corresponding SNR_q can be computed for each exposure. It should be emphasized that in the present implementation, the annular pupil performs the first iteration of image spectrum manipulation by accentuating certain spatial frequencies, whereas the exposure time controls the necessary level of signal amplification/attenuation to transfer a right amount of auxiliary contribution to the image plane. The annular pupil with varied photon exposure, in effect, directly produces the required auxiliary (Eq. (20)) of the object plane as minted into the compound object-auxiliary pattern proportional to the exposure time. The level of exposure and the annular pupil dimensions are determined care-

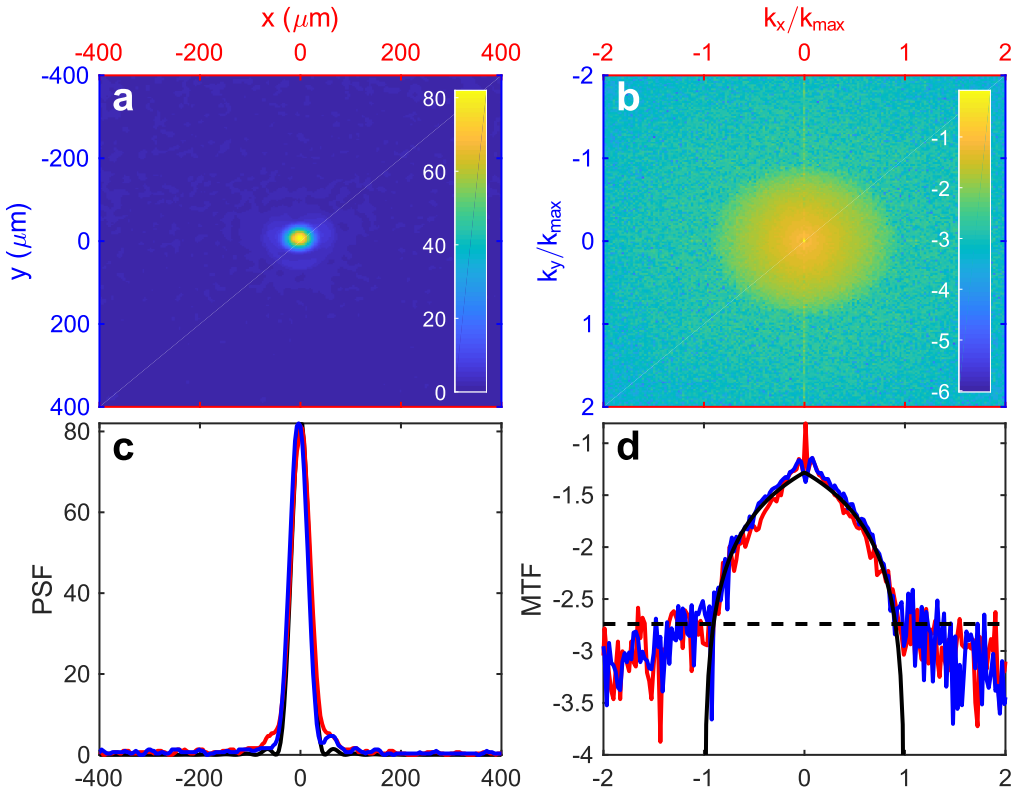

FIG. 3. Measured PSF and MTF for full, unobstructed pupil with NA= 0.0066 and exposure time of $T = 2$ s. (a) The PSF collected from the setup in Fig. 2. (b) The MTF calculated by fast Fourier transformation of part (a) in log scale. (c) Cross-sections of part (a) through the origin along x (red line) and y (blue line). The theoretical prediction is given by the black line. (d) Cross-sections of part (b) through the origin along k_x (red line) and k_y (blue line). The theoretical prediction is given by the solid black line. The dashed black line denotes the calculated shot noise standard deviation using Eq. (8).

fully from the limiting spatial frequency of the reference system and the fact that *shot noise variance is constant and equal to the total expected number of photons* (Eq. (8)).

Examples of the experimentally measured PSFs and MTFs, with the same scaling factor as the PSFs, are presented in Figs. 3 and 4 for the open and annular pupils, respectively. Also shown are the theoretical PSFs and MTFs determined from scalar diffraction theory. A good agreement can be seen with both the PSF and MTF between theory (black lines) and experiment (red and blue lines), indicating that the imaging system is well aligned and not inducing any unwanted aberrations. Also, the calculated standard deviation (black dashed line) seems to accurately predict where the MTF signal is overcome by the shot noise, providing evidence supporting the theoretical model for spectral noise. Since $\sigma_e = 0$ in this calculation, it is apparent that the readout noise is in fact likely negligible.

From the OTFs computed from the measured PSFs in Figs. 3 and 4, it is then straightforward to compute SNR_q for each exposure using Eq. (15), assuming that the experimental pixel values and the number of photons at each pixel are about linearly related. These are plotted in Fig. 5(a), where the solid lines indicate the open pupil SNR_q and the dashed lines indicate the annular pupil SNR_q. For a direct comparison of the SNR_q for the two pupil configurations, we define a spectral SNR improvement metric

$$\mathrm{SNRi}_q = \frac{\mathrm{SNR}_{q,a,T}}{\mathrm{SNR}_{q,o,T_0}}, \tag{21}$$

where $\mathrm{SNR}_{q,a,T}$ is the annular pupil spectral SNR for exposure time T and SNR_{q,o,T_0} is the open pupil spectral SNR for exposure time T_0. Plotted in Fig. 5(b) is the SNRi_q for $T_0 = 2$ s and three different values of T. It can be seen that a clear enhancement in the SNR for spatial frequencies near $0.83k_{max}$ can be obtained using an annular pupil provided a sufficient exposure.

To verify that the high spatial frequency improvement in spectral SNR with sufficient exposure manifests as improved image resolution, we imaged a USAF-1951 resolution test target (Thorlabs R1DS1N) using the setup in Fig. 2(a). The collected images for the open and annular pupil are shown in Fig. 6 for different values of T. Also shown are the corresponding reconstructions obtained by

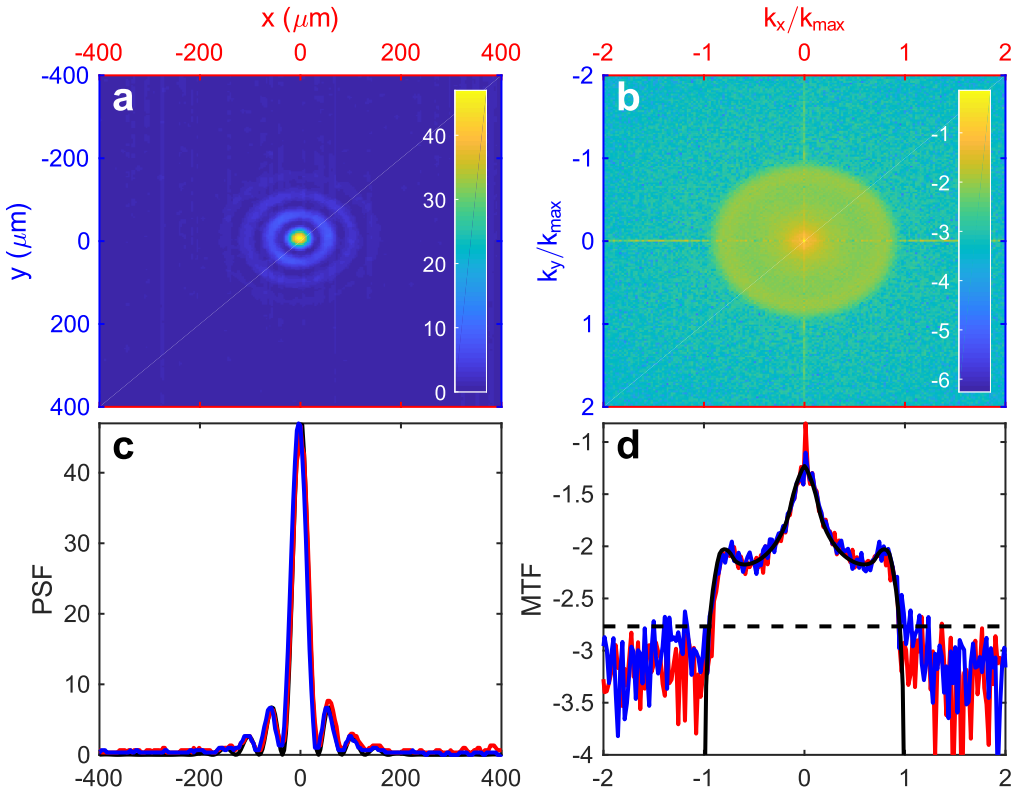

FIG. 4. Measured PSF and MTF for annular pupil with $k_- = k_{max}/2\sqrt{2}$, NA= 0.0066, and exposure time of $T = 4$ s. The subfigures are defined in the same manner as Fig. 3.

deconvolving the raw images with the Richardson-Lucy algorithm [39, 40] after 30 iterations as implemented in MATLAB. In Figs. 6(a)-(c), it can be seen that three-bar target in element 5 is always blurred together by the open pupil (red solid rectangles), however even for low exposure (e.g. $T = 10$ ms), the bars become qualitatively visible in the annular pupil case (yellow solid rectangles). After reconstruction for 30 iterations, element 5 remains unresolved in the open pupil images (red dashed rectangles), but the annular pupil images of element 5 are further improved (yellow dashed rectangles).

When the exposure time T is increased, the spectral SNR for the experimental MTF (Figs. 3 and 4) is scaled by a factor of $\sqrt{T}$ (Eqs. (3) and (15)) as long as no pixel saturation takes place. Particularly, as shown in Fig. 5, the annular pupil selectively amplifies the amplitudes of the spatial frequencies within a specific range and improves the spectral SNR in that region even beyond the point which may not be otherwise possible due to the pixel saturation with the open pupil (i.e., the reference system). This enhancement may occur at the expense of reduced spectral SNR at the other regions (e.g., lower spatial frequencies). However, those regions may be recovered easily with deconvolution. Particularly for elements 2-4 in Figs. 6(a)-(c), the annular pupil image is improved greatly by the reconstruction since those spatial frequencies were originally attenuated with respect to the open pupil. Importantly, since the spectral noise variance is equal to the total expected number of photons in the entire image (Eq. (8)), it is indeed advantageous to suppress the energy-rich regions so that the selective amplification successfully delivers power to the most demanding spectral band without (excessively) amplifying the noise. As a result, such a noise behavior driven spectrum manipulation, critical to the implementation of the ACI, enables us to push the SNR limit for the reference imaging system and significantly enhance the overall image contrast and resolution as can be clearly seen in Figs. 6(a)-(c). The improvement is prominent if, for instance, element 5 (both the raw and deconvolved images) obtained from the open pupil with $T = 10$ ms is compared with that of the annular pupil with $T = 50$ ms. Conversely, if element 5 obtained from the open pupil with $T = 50$ ms is compared with that of the annular pupil with $T = 10$ ms, it is also observed that the ACI can achieve higher resolution and contrast with shorter exposure—a highly desirable feature for bioimaging modalities to avoid photo-damage [42–44, 46, 47, 53] to the sample or eye-safe operations.

Next, in Fig. 6(d), we delve into an extreme case

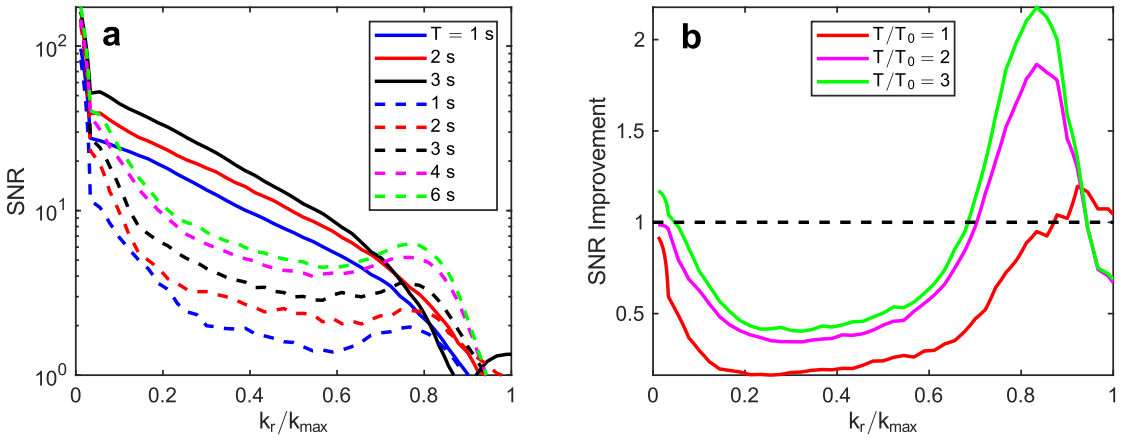

FIG. 5. Improvement in spectral SNR. (a) Measured spectral SNR for open (solid lines) and annular (dashed lines) pupils for different exposure times. The crossover by the black solid line over the red and blue lines is due to distortion of the PSF by pixel saturation at $T = 3$ s for the open pupil. (b) Spectral SNR improvement SNRi_q corresponding to the data in part (a) with $T_0 = 2$ s. The black dashed line indicates $\mathrm{SNRi}_q = 1$.

of photon exposure whereupon pixel saturation occurs. Upon viewing the open pupil SNR_q from Eqs. (3) and (15), nonetheless, it would seem that simply increasing T would lead to an improvement in SNR_q itself, without having to modify the pupil. However, the pixels in typical digital cameras only have finite well depth and dynamic range, meaning they can experience saturation for long exposures and/or intense illumination. The saturation causes a nonlinear response of the pixel as a function of the input photon signal. Therefore, one cannot arbitrarily increase T or illumination intensity to increase SNR_q. In terms of spatial resolution, saturation can manifest as an effective blurring due to clipping of the pixel values and blooming of photoelectrons to adjacent pixels.

Along with provided improved resolution and contrast, the proposed spectrum manipulation method can also provide resistance to pixel saturation in cases when long exposure or intense illumination *and* high resolution is required. To demonstrate this, we collected images in which the pixels become saturated for the open pupil system, and compared them to images in the annular pupil system. They are shown in Fig. 6(d). Clearly, the annular pupil has higher resistance to pixel saturation than the open pupil, despite twice longer exposure time. Element 5 can never be resolved with the open pupil as the pixel saturation appears earlier. A larger portion of the Fourier space is blocked by the annular pupil. As evidenced by Fig. 2(d), the blocked photons correspond to lower spatial frequencies which are more likely to contribute to pixel saturation, since the transmission for these portions of the object will be high due to the larger local photon flux. Therefore, a cleverly tuned selective amplification does not only improve the resolution and contrast, but also renders the imaging system more immune to the pixel saturation.

IV. DISCUSSION AND CONCLUSIONS

In this work, it was demonstrated experimentally for the first time that the active convolved illumination enhances the SNR, image resolution, and contrast. This method utilizes manipulation of the Fourier space by employing an auxiliary, which both relies on the noise behaviour and correlates with the object pattern, in order to tame the image spectrum SNR. Here, this is simply achieved by an annular pupil and an embedded auxiliary with a variable exposure time. Placing an annular pupil transparency in the pupil plane while adjusting the photon exposure leads to improved SNR for larger spatial frequencies, which gives improved resolution over an imaging system with unobstructed pupil and the same numerical aperture. Also, the annular pupil increases resistance to pixel saturation, since a portion of the Fourier space is blocked and the number of photons at the detector is decreased. The theory and simulation of the proposed loss mitigation and resolution enhancement method for incoherent light, the experiment to verify and expand upon the previous metamaterial implementations at near-field [2, 27, 31–34], and how to manipulate the pupil or OTF of an imaging system to achieve a desired high spatial frequency SNR have been discussed. The choice for the small NA in this proof-of-principle experiment was made mostly for practical reasons dictated by our bar target and achromatic doublet lenses. There is no theoretical limitation to applying this concept to a high-NA system like a microscope objective. As long as there is access to the Fourier space, one can still modify the pupil function.

The spatial filtering properties of annular pupil is well-known and commonly used in imaging systems [54]. However, the motivation in our work is different in that we solely use the annular pupil to prove experimentally that

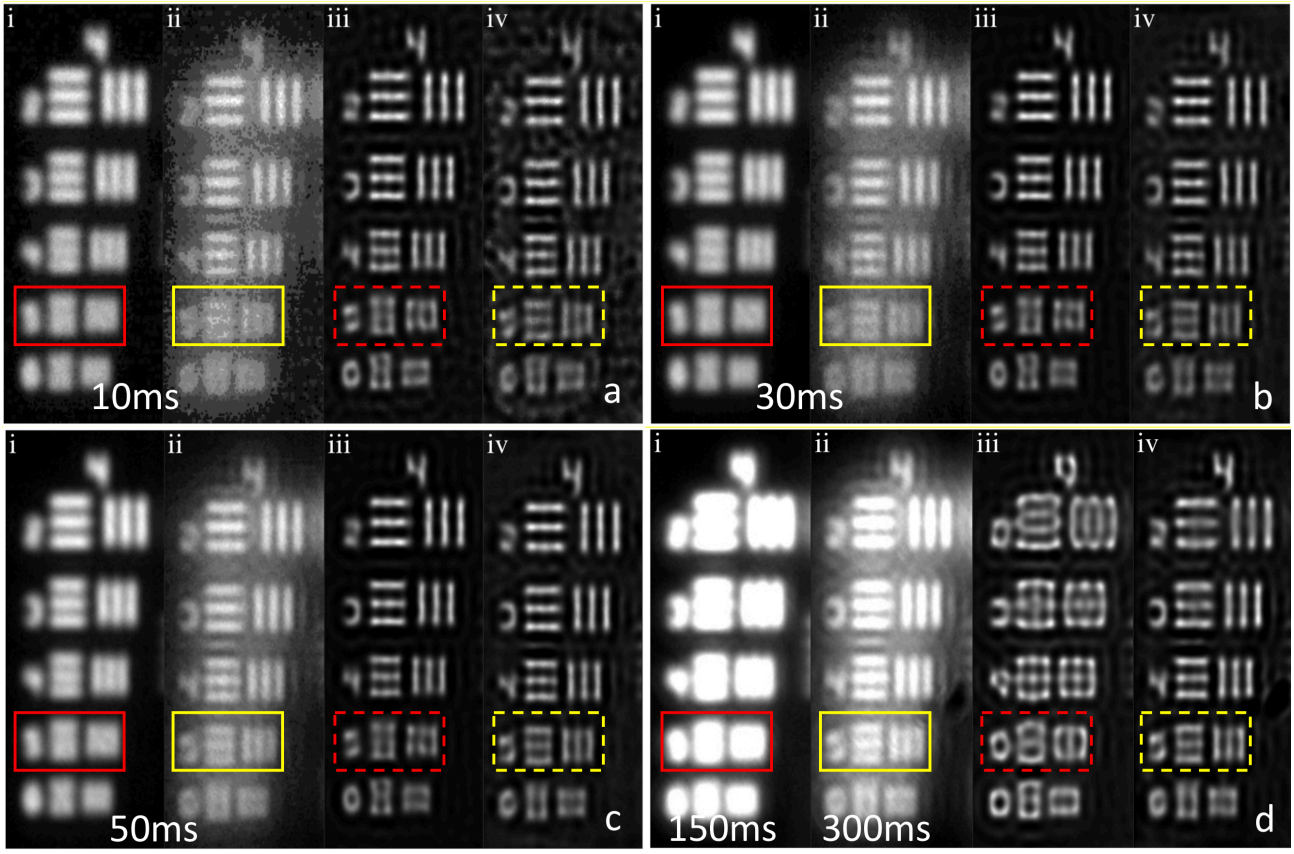

FIG. 6. Experimental images of a USAF-1951 resolution test target collected from the setup in Fig. 2. (a) $T = 10$ ms, (b) $T = 30$ ms, and (c) $T = 50$ ms exposure times. The individual images in each subfigure correspond to the following: i. Raw image collected with open pupil in the pupil plane and NA=0.0066. ii. Raw image with annular pupil in the pupil plane and same NA as i. iii. Image from subpart i deconvolved by the Richardson-Lucy algorithm after 30 iterations. iv. Image from subpart ii deconvolved by the Richardson-Lucy algorithm after 30 iterations. Red rectangles highlight the raw (solid) and deconvolved (dashed) images for element 5 using the open pupil. Similarly, the yellow rectangles do so for the annular pupil. Clear improvement in image resolution and contrast is seen with the annular pupil. (d) Images demonstrating the resistance of annular pupil to deleterious effects caused by detector saturation. Subparts i-iv and the rectangles are defined similar to parts (a)-(c). For the open pupil, $T = 150$ ms, and for the annular pupil, $T = 300$ ms. It can be seen that even for twice as long exposure time, the annular pupil image quality is mostly maintained compared to the open pupil image, which is severely blurred due to pixel saturation. The ACI is implemented with annular pupil and varied photon exposure, and the reference system with open pupil.

the ACI concept, which has only been proposed theoretically so far, indeed works. To achieve that, we find one specific implementation that is mathematically equivalent to the previous theoretical implementations of the ACI. We choose the annular pupil with a controlled exposure time as a simple and convenient tool for this purpose. It is not our intention here to find an optimal or a unique implementation of the ACI as this would require a sophisticated spectral engineering (e.g., using machine learning and meta-optics) specifically optimized for the imaging system of interest with specific noise or distortion statistics. Instead, considering the implementation with the annular pupil and controlled exposure time as a simple example or case of ACI, our manuscript presents the first experimental evidence that the ACI idea is indeed well-founded. This represents the novelty in our manuscript.

Similarly, spatial filtering with a central obscuration to block low spatial frequencies to achieve increased spectral SNR at higher spatial frequencies of the diffracted beam and avoid pixel saturation from the direct beam, such as in X-ray coherent diffraction imaging (CDI) [53], or for edge enhancement in different coherent imaging modalities may be regarded as a simple and special case of coherent ACI [2]. In general, more sophisticated use of ACI with clever illumination structuring [55] driven by the noise statistics [2] may deliver more favorable results in diverse imaging systems. For example, such a structured illumination source immune to noise may improve the X-ray CDI measurements and the performance of reconstruction algorithms [56–58] by controlling the coherence of the incident illumination [58–60].

It is worth mentioning that the implementation of ACI presented here should not be confused with incoherent edge detection as the latter usually relies on bipolar incoherent image processing [61–63]. Also, although some of our methodologies are inspired by the recent split-pupil-optimization technique [4], the proposed technique here is more general, does not contend with a constant photon budget, and is intimately connected with the virtual gain phenomenon in an earlier theoretical proposal [27] as illustrated schematically in Fig. 1(b). The ACI offers new opportunities for not only conventional imaging systems and superlenses, but also various other linear systems. One can envision its potential generalization and ubiquity to encompass imaging through random media (e.g., turbulent and scattering atmosphere) [64–68], spectroscopy [69], $\mathcal{PT}$-symmetry [28, 70, 71], photolithography [10, 11], and quantum information and image processing [72–74]. The virtual gain mechanism employed in ACI can alleviate the stringent requirement of balance between loss and gain in $\mathcal{PT}$-symmetric systems [28]. It is important to note that the systems with more intricate noise/distortion characteristics (e.g., turbulent atmosphere) may necessitate more ingenious engineering of the pupil function than here. Optimal and precise manipulation of the pupil function, beyond conventional optics, may be possible with the advent of amenable metasurfaces [14–16]. More work on ACI and potential relevance with SIM [3, 41–44], superoscillatory imaging [74–77], and super-gain [78] can enrich further understanding of imaging beyond the known boundaries. Computational superresolution techniques [35–37, 49, 50] integrated with ACI enabled systems can provide extended resolution limits. Machine learning approaches [35] bolstered with ACI may enable optical visualization of dynamic scenes at previously inaccessible scales. An interesting direction of research could be utilizing the analytical continuity principle [35–37] while enhancing the SNR with ACI to achieve far-field super-resolution imaging. Since ACI is fundamentally a physical process (i.e., physical preprocessing) that enhances speed, over time-consuming deconvolution, and data acquisition, it may benefit numerous imaging scenarios. It may also be possible to use cheap detectors and yet obtain the same imaging quality as that of expensive ones not aided by ACI.

ACKNOWLEDGEMENTS

This work was supported by the Office of Naval Research (N00014-15-1-2684) and the National Science Foundation (EAR-2221730). The authors would like to thank Christopher Middlebrook at Michigan Technological University for fruitful discussions.

[1] Joseph W. Goodman, *Introduction to Fourier Optics* (Roberts and Company Publishers, 2005).
[2] Anindya Ghoshroy, Wyatt Adams, and Durdu Ö Güney, "Theory of coherent active convolved illumination for superresolution enhancement," J. Opt. Soc. Am. B **37**, 2452–2463 (2020).
[3] E. A. Ingerman, R. A. London, R. Heintzmann, and M. G. L. Gustafsson, "Signal, noise and resolution in linear and nonlinear structured-illumination microscopy," Journal of Microscopy **273**, 3–25 (2019).
[4] Jan Becker, Ronny Förster, and Rainer Heintzmann, "Better than a lens - A novel concept to break the SNR-limit, given by Fermat's principle," arXiv:1811.08267 [physics] (2018), arXiv: 1811.08267.
[5] Wyatt Adams, Mehdi Sadatgol, and Durdu Ö. Güney, "Review of near-field optics and superlenses for sub-diffraction-limited nano-imaging," AIP Advances **6**, 100701 (2016).
[6] Joseph L. Ponsetto, Anna Bezryadina, Feifei Wei, Keisuke Onishi, Hao Shen, Eric Huang, Lorenzo Ferrari, Qian Ma, Yimin Zou, and Zhaowei Liu, "Experimental demonstration of localized plasmonic structured illumination microscopy," ACS Nano **11**, 5344–5350 (2017).
[7] Qian Ma, Huan Hu, Eric Huang, and Zhaowei Liu, "Super-resolution imaging by metamaterial-based compressive spatial-to-spectral transformation," Nanoscale **9**, 18268–18274 (2017).
[8] Anna Bezryadina, Junxiang Zhao, Yang Xia, Xiang Zhang, and Zhaowei Liu, "High spatiotemporal resolution imaging with localized plasmonic structured illumination microscopy," ACS Nano **12**, 8248–8254 (2018).
[9] Yeon Ui Lee, Junxiang Zhao, Qian Ma, Larousse Khosravi Khorashad, Clara Posner, Guangru Li, G Bimananda M Wisna, Zachary Burns, Jin Zhang, and Zhaowei Liu, "Metamaterial assisted illumination nanoscopy via random super-resolution speckles," Nature Communications **12**, 1559 (2021).
[10] Ping Gao, Na Yao, Changtao Wang, Zeyu Zhao, Yunfei Luo, Yanqin Wang, Guohan Gao, Kaipeng Liu, Chengwei Zhao, and Xiangang Luo, "Enhancing aspect profile of half-pitch 32 nm and 22 nm lithography with plasmonic cavity lens," Applied Physics Letters **106**, 093110 (2015).
[11] Gaofeng Liang, Xi Chen, Qing Zhao, and L. Jay Guo, "Achieving pattern uniformity in plasmonic lithography by spatial frequency selection," Nanophotonics **7**, 277–286 (2018).
[12] Liming Si, Haixin Jiang, Xin Lv, and Jun Ding, "Broadband extremely close-spaced 5G MIMO antenna with mutual coupling reduction using metamaterial-inspired superstrate," Optics Express **27**, 3472–3482 (2019).
[13] Wei Yang and Yu-Sheng Lin, "Tunable metamaterial filter for optical communication in the terahertz frequency range," Optics Express **28**, 17620–17629 (2020).
[14] You Zhou, Ivan I. Kravchenko, Hao Wang, Hanyu Zheng, Gong Gu, and Jason Valentine, "Multifunctional metaoptics based on bilayer metasurfaces," Light: Science & Applications **8**, 80 (2019).
[15] You Zhou, Hanyu Zheng, Ivan I. Kravchenko, and Jason Valentine, "Flat optics for image differentiation," Nature Photonics **14**, 316–323 (2020).

[16] Junsuk Rho, "Metasurfaces: Subwavelength nanostructure arrays for ultrathin flat optics and photonics," MRS Bulletin **45**, 180–187 (2020).

[17] Sourangsu Banerji, Monjurul Meem, Apratim Majumder, Fernando Guevara Vasquez, Berardi Sensale-Rodriguez, and Rajesh Menon, "Imaging with flat optics: metalenses or diffractive lenses?" Optica **6**, 805–810 (2019).

[18] Sergey Krasikov, Aaron Tranter, Andrey Bogdanov, and Yuri Kivshar, "Intelligent metaphotonics empowered by machine learning," Opto-Electron. Adv. **5**, 210147 (2022).

[19] Antonino Calà Lesina, Dominic Goodwill, Eric Bernier, Lora Ramunno, and Pierre Berini, "Tunable plasmonic metasurfaces for optical phased arrays," IEEE Journal of Selected Topics in Quantum Electronics **27**, 4700116 (2020).

[20] Roberto Zecca, Daniel L. Marks, and David R. Smith, "Symphotic design of an edge detector for autonomous navigation," IEEE Access **7**, 144836–144844 (2019).

[21] S. A. Uriri, T. Tashima, X. Zhang, M. Asano, M. Bechu, D. Ö. Güney, T. Yamamoto, Ş. K. Özdemir, M. Wegener, and M. S. Tame, "Active control of a plasmonic metamaterial for quantum state engineering," Physical Review A **97**, 053810 (2018).

[22] Mohammad Mirhosseini, Eunjong Kim, Vinicius S. Ferreira, Mahmoud Kalaee, Alp Sipahigil, Andrew J. Keller, and Oskar Painter, "Superconducting metamaterials for waveguide quantum electrodynamics," Nature Communications **9**, 3706 (2018).

[23] Jacob B. Khurgin and Greg Sun, "In search of the elusive lossless metal," Applied Physics Letters **96**, 181102 (2010).

[24] Alex Krasnok and Andrea Alù, "Active nanophotonics," Proceedings of the IEEE **108**, 628–654 (2020).

[25] Anindya Ghoshroy, Şahin K. Özdemir, and Durdu Ö. Güney, "Loss compensation in metamaterials and plasmonics with virtual gain," Optical Materials Express **10**, 1862–1880 (2020).

[26] Eric O. Potma, Conor Evans, X. Sunney Xie, R. Jason Jones, and Jun Ye, "Picosecond-pulse amplification with an external passive optical cavity," Optics Letters **28**, 1835–1837 (2003).

[27] Mehdi Sadatgol, Şahin K. Özdemir, Lan Yang, and Durdu Ö. Güney, "Plasmon injection to compensate and control losses in negative index metamaterials," Physical Review Letters **115**, 035502 (2015).

[28] Huanan Li, Ahmed Mekawy, Alex Krasnok, and Andrea Alù, "Virtual parity-time symmetry," Physical Review Letters **124**, 193901 (2020).

[29] Wyatt Adams, Mehdi Sadatgol, Xu Zhang, and Durdu Ö. Güney, "Bringing the 'perfect lens' into focus by near-perfect compensation of losses without gain media," New Journal of Physics **18**, 125004 (2016).

[30] Xu Zhang, Wyatt Adams, and Durdu Ö. Güney, "Analytical description of inverse filter emulating the plasmon injection loss compensation scheme and implementation for ultrahigh-resolution hyperlens," J. Opt. Soc. Am. B **34**, 1310–1318 (2017).

[31] Anindya Ghoshroy, Wyatt Adams, Xu Zhang, and Durdu Ö. Güney, "Active plasmon injection scheme for subdiffraction imaging with imperfect negative index flat lens," J. Opt. Soc. Am. B **34**, 1478–1488 (2017).

[32] Wyatt Adams, Anindya Ghoshroy, and Durdu Ö. Güney, "Plasmonic superlens imaging enhanced by incoherent active convolved illumination," ACS Photonics **5**, 1294–1302 (2018).

[33] Anindya Ghoshroy, Wyatt Adams, Xu Zhang, and Durdu Ö. Güney, "Hyperbolic metamaterial as a tunable near-field spatial filter to implement active plasmon-injection loss compensation," Physical Review Applied **10**, 024018 (2018).

[34] Anindya Ghoshroy, Wyatt Adams, Xu Zhang, and Durdu Ö Güney, "Enhanced superlens imaging with loss-compensating hyperbolic near-field spatial filter," Optics Letters **43**, 1810–1813 (2018).

[35] Hongda Wang, Yair Rivenson, Yiyin Jin, Zhensong Wei, Ronald Gao, Harun Günaydın, Laurent A. Bentolila, Comert Kural, and Aydogan Ozcan, "Deep learning enables cross-modality super-resolution in fluorescence microscopy," Nature Methods **16**, 103–110 (2019).

[36] I. J. Cox and C. J. R. Sheppard, "Information capacity and resolution in an optical system," J. Opt. Soc. Am. A **3**, 1152–1158 (1986).

[37] Y. Katznelson, *An Introduction to Harmonic Analysis* (Dover Publications, 1976).

[38] Michael C. Roggemann, David W. Tyler, and Marsha F. Bilmont, "Linear reconstruction of compensated images: theory and experimental results," Applied Optics **31**, 7429–7441 (1992).

[39] William Hadley Richardson, "Bayesian-based iterative method of image restoration," J. Opt. Soc. Am. **62**, 55–59 (1972).

[40] Leon B. Lucy, "An iterative technique for the rectification of observed distributions," The Astronomical Journal **79**, 745 (1974).

[41] Lothar Schermelleh, Alexia Ferrand, Thomas Huser, Christian Eggeling, Markus Sauer, Oliver Biehlmaier, and Gregor P. C. Drummen, "Super-resolution microscopy demystified," Nature Cell Biology **21**, 72–84 (2019).

[42] Peter Kner, Bryant B. Chhun, Eric R. Griffis, Lukman Winoto, and M. G. L. Gustafsson, "Super-resolution video microscopy of live cells by structured illumination," Nature Methods **6**, 339–342 (2009).

[43] Andrew G. York, Sapun H. Parekh, Damian Dalle Nogare, Robert S. Fischer, Kelsey Temprine, Marina Mione, Ajay B. Chitnis, Christian A. Combs, and Hari Shroff, "Resolution doubling in live, multicellular organisms via multifocal structured illumination microscopy," Nature Methods **9**, 749–754 (2012).

[44] Andrew G. York, Panagiotis Chandris, Damian Dalle Nogare, Jeffrey Head, Peter Wawrzusin, Robert S. Fischer, Ajay Chitnis, and Hari Shroff, "Instant super-resolution imaging in live cells and embryos via analog image processing," Nature Methods **10**, 1122–1126 (2013).

[45] Eva Wegel, Antonia Göhler, B. Christoffer Lagerholm, Alan Wainman, Stephan Uphoff, Rainer Kaufmann, and Ian M. Dobbie, "Imaging cellular structures in super-resolution with SIM, STED and localisation microscopy: a practical comparison," Scientific Reports **6**, 27290 (2016).

[46] F. Bottanelli, E. B. Kromann, E. S. Allgeyer, R. S. Erdmann, S. W. Baguley, G. Sirinakis, A. Schepartz, D. Baddeley, D. K. Toomre, J. E. Rothman, and J. Bewersdorf,

"Two-colour live-cell nanoscale imaging of intracellular targets," Nature Communications **7**, 10778 (2016).

[47] Sara A. Jones, Sang-Hee Shim, Jiang He, and Xiaowei Zhuang, "Fast, three-dimensional super-resolution imaging of live cells," Nature Methods **8**, 499–505 (2011).

[48] H. Takakura, Y. Zhang, R. S. Erdmann, A. D. Thompson, Y. Lin, B. McNellis, F. Rivera-Molina, S.-N. Uno, M. Kamiya, Y. Urano, J. E. Rothman, J. Bewersdorf, A. Schepartz, and D. Toomre, "Long time-lapse nanoscopy with spontaneously blinking membrane probes," Nature Biotechnology **35**, 773–780 (2017).

[49] Mario Bertero and Patrizia Boccacci, "Super-resolution in computational imaging," Micron **34**, 265–273 (2003).

[50] Zhi-ping Zeng, Hao Xie, Long Chen, Karl Zhanghao, Kun Zhao, Xu-san Yang, and Peng Xi, "Computational methods in super-resolution microscopy," Frontiers of Information Technology & Electronic Engineering **18**, 1222–1235 (2017).

[51] Trevor Hastie, Robert Tibshirani, and Jerome Friedman, *The Elements of Statistical Learning* (Springer, 2016).

[52] W. Adams, C. Kendrick, C. T. Middlebrook, and D. O. Guney, "Balancing the photo-budget in far-field optical imaging for enhanced lateral resolution," in *The 10th International Conference on Metamaterials, Photonic Crystals and Plasmonics* (2019) p. 511.

[53] Jianwei Miao, Richard L. Sandberg, and Changyong Song, "Coherent X-ray diffraction imaging," IEEE Journal of Selected Topics in Quantum Electronics **18**, 399–410 (2011).

[54] Yaping Zhang, Ting-Chung Poon, Peter W. M. Tsang, Rende Wang, and Lin Wang, "Review on feature extraction for 3-D incoherent image processing using optical scanning holography," IEEE Transactions on Industrial Informatics **15**, 6146 (2019).

[55] Y. J. Liu, B. Chen, E. R. Li, J. Y. Wang, A. Marcelli, S. W. Wilkins, H. Ming, Y. C. Tian, K. A. Nugent, P. P. Zhu, and Z. Y. Wu, "Phase retrieval in x-ray imaging based on using structured illumination," Physical Review A **78**, 023817 (2008).

[56] Pierre Godard, Marc Allain, Virginie Chamard, and John Rodenburg, "Noise models for low counting rate coherent diffraction imaging," Optics Express **20**, 25914–25934 (2012).

[57] Timur E. Gureyev, Alexander Kozlov, Yakov I. Nesterets, David M. Paganin, Andrew V. Martin, and Harry M. Quiney, "Signal-to-noise, spatial resolution and information capacity of coherent diffraction imaging," IUCrJ **5**, 716–726 (2018).

[58] Bo Chen, Brian Abbey, Ruben Dilanian, Eugeniu Balaur, Grant Van Riessen, Mark Junker, Chanh Q. Tran, Michael W. M. Jones, Andrew G. Peele, Ian McNulty, David J. Vine, Corey T. Putkunz, Harry M. Quiney, and Keith A. Nugent, "Diffraction imaging: The limits of partial coherence," Physical Review B **86**, 235401 (2012).

[59] Garth J. Williams, Harry M. Quiney, Andrew G. Peele, and Keith A. Nugent, "Coherent diffractive imaging and partial coherence," Physical Review B **75**, 104102 (2007).

[60] Yuanyuan Liu, Qingwen Liu, Shuangxiang Zhao, Wenchen Sun, Bingxin Xu, and Zuyuan He, "Resolution enhancement in coherent diffraction imaging using high dynamic range image," Photonics **8**, 370 (2021).

[61] P. Bhuvaneswari and A. Brindha Therese, "Edge detection techniques in digital and optical image processing," Int. J. Eng. Res. Appl. **4**, 33–37 (2014).

[62] A. W. Lohmann and William T. Rhodes, "Two-pupil synthesis of optical transfer functions," Applied Optics **17**, 1141–1151 (1978).

[63] Yaping Zhang, Rende Wang, Peter Tsang, and Ting-Chung Poon, "Sectioning with edge extraction in optical incoherent imaging processing," OSA Continuum **3**, 698–708 (2020).

[64] Larry C. Andrews, *Laser Beam Propagation through Random Media* (SPIE, 2005).

[65] Halil T. Eyyuboğlu, Yahya Baykal, Emre Sermutlu, and Yangjian Cai, "Scintillation advantages of lowest order Bessel-Gaussian beams," Applied Physics B **92**, 229–235 (2008).

[66] Mohamed E. Hanafy, Michael C. Roggemann, and Durdu O. Guney, "Detailed effects of scattering and absorption by haze and aerosols in the atmosphere on the average point spread function of an imaging system," J. Opt. Soc. Am. A **31**, 1312–1319 (2014).

[67] Mohamed E. Hanafy, Michael C. Roggemann, and Durdu O. Guney, "Estimating the image spectrum signal-to-noise ratio for imaging through scattering media," Optical Engineering **54**, 013102 (2015).

[68] Mohamed E. Hanafy, Michael C. Roggemann, and Durdu O. Guney, "Reconstruction of images degraded by aerosol scattering and measurement noise," Optical Engineering **54**, 033101 (2015).

[69] Hichem Guerboukha, Kathirvel Nallappan, and Maksim Skorobogatiy, "Toward real-time terahertz imaging," Advances in Optics and Photonics **10**, 843–938 (2018).

[70] Francesco Monticone, Constantinos A. Valagiannopoulos, and Andrea Alù, "Parity-time symmetric nonlocal metasurfaces: all-angle negative refraction and volumetric imaging," Physical Review X **6**, 041018 (2016).

[71] Ramy El-Ganainy, Mercedeh Khajavikhan, Demetrios N. Christodoulides, and Sahin K. Ozdemir, "The dawn of non-Hermitian optics," Communications Physics **2**, 37 (2019).

[72] A. B. Mikhalychev, B. Bessire, I. L. Karuseichyk, A. A. Sakovich, M. Unternährer, D. A. Lyakhov, Dominik L. Michels, A. Stefanov, and D. Mogilevtsev, "Efficiently reconstructing compound objects by quantum imaging with higher-order correlation functions," Communications Physics **2**, 134 (2019).

[73] Thomas Gregory, P.-A. Moreau, Ermes Toninelli, and Miles J. Padgett, "Imaging through noise with quantum illumination," Science Advances **6**, eaay2652 (2020).

[74] Guang Hui Yuan, Stefano Vezzoli, Charles Altuzarra, Edward T. F. Rogers, Christophe Couteau, Cesare Soci, and Nikolay I. Zheludev, "Quantum super-oscillation of a single photon," Light: Science & Applications **5**, e16127–e16127 (2016).

[75] Guanghui Yuan, Katrine S Rogers, Edward T. F. Rogers, and Nikolay I. Zheludev, "Far-field superoscillatory metamaterial superlens," Physical Review Applied **11**, 064016 (2019).

[76] Tanchao Pu, Jun-Yu Ou, Nikitas Papasimakis, and Nikolay I. Zheludev, "Label-free deeply subwavelength optical microscopy," Applied Physics Letters **116**, 131105 (2020).

[77] Gang Chen, Zhong-Quan Wen, and Cheng-Wei Qiu, "Superoscillation: from physics to optical applications," Light: Science & Applications **8**, 56 (2019).

[78] G. Di Francia, "Directivity, super-gain and information," IRE Transactions on Antennas and Propagation **4**, 473–

478 (1956).